This is a preproof accepted article for *Mineralogical Magazine*
This version may be subject to change during the production process
Doi: 10.1180/mgm.2025.10081

Extending the mineralogy of U^{6+} (II.): Barronite, a new uranyl silicate related to weeksite from Menzenschwand, Germany#

JAKUB PLÁŠIL[1*], GWLADYS STECIUK[2], RADEK ŠKODA[3], JIŘÍ SEJKORA[4], ZDENĚK DOLNÍČEK[4], NICOLAS MEISSER[5], STEFAN ANSERMET[5], AND CARSTEN SLOTTA[6]

[1] Institute of Physics of the CAS, Na Slovance 2, 182 21 Prague 8, Czech Republic
[2] Université de Lorraine, CNRS UMR UMR 7198, Institut Jean Lamour, 54000 Nancy, France
[3] Department of Geological Sciences, Masaryk University, Kotlářská 2, 61137 Brno, Czech Republic
[4] Department of Mineralogy and Petrology, National Museum, Cirkusová 1740, 193 00 Prague 9, Czech Republic
[5] Département de géologie, Muséum cantonal des sciences naturelles (Naturéum), Université de Lausanne (UNIL), Anthropole, 1015 Lausanne, Switzerland
[6] Mintreasure.com, independent researcher

*Corresponding author; Email: plasil@fzu.cz

Abstract

The new mineral barronite (IMA 2024-053), $(\square_{1.5}Ba_{0.5})_2(UO_2)_2Si_5O_{12}(OH) \cdot 2H_2O$, was found in the material from Menzenschwand uranium deposit, Black Forest Mts., Germany, where it occurs as globular/acicular aggregates, consisting of long-prismatic crystals, up to 0.3 mm in length, in baryte and quartz-based gangue. Barronite is not associated with any other supergene minerals. Crystals are pale yellow with colourless to pale yellow streak. Nevertheless, some of the crystals have a brown-orange tint, caused by Fe-Si-gels. The tenacity is brittle, the Mohs hardness is 1–2. The mineral has distinct cleavage on {100}; the fracture is uneven. Barronite is biaxial (+), with $\alpha = 1.599(2)$, $\beta = 1.607(2)$, $\gamma = 1.617(3)$; $2V$ (meas.) = 86°. Optical orientation is X = **b**, $Y \wedge$ **a** ~3° in the obtuse angle β. Dispersion is distinct $r>v$. Pleochroism is distinct in hues of pale-yellow $X<Y<Z$. Electron microprobe analyses provided (based on 19 O atoms) $(\square_{1.369}Ba_{0.345}K_{0.165}Ca_{0.086}Pb_{0.024}Fe_{0.011})_{\Sigma 2.000}(U_{0.996}O_2)_2Si_{4.989}O_{12}(OH) \cdot 2H_2O$. Barronite is monoclinic, $C2/m$, a = 14.2115(11) Å, b = 14.0169(19) Å, c = 9.6545(8) Å, β = 111.59(6)°, with V = 1788.2(8) Å^3 (Z = 4), refined from the corrected 3D ED data at 94K. The crystal structure refinement (R_1 = 0.0791 for 6596 [$I > 3\sigma(I)$] reflections) refined from the 3D ED data confirmed that barronite has the same structural architecture as weeksite; however, it contains less H_2O in the channels of the uranyl-silicate framework structure.

https://doi.org/10.1180/mgm.2025.10081 Published online by Cambridge University Press

Keywords: barronite, uranyl silicate, new mineral, crystal structure, 3D electron diffraction, complexity, weeksite topology.

Introduction

The new mineral barronite, ideally $(\square_{1.5}Ba_{0.5})_2(UO_2)_2Si_5O_{12}(OH) \cdot 2H_2O$, is named after the exploration geologist Keith Barron (born 1962), the winner of the Thayer Lindsay award (2008) for his discovery of the famous Au-Ag deposit of Fruta del Norte in Ecuador, owner of the second world's largest sapphire mine of Rock Creek, Montana, USA, and actively exploring gold, copper, base metal and uranium in Switzerland, Argentina, Ecuador, Guyana and France. The new mineral and its name have been approved by the Commission on New Minerals, Nomenclature and Classification of the International Mineralogical Association (IMA 2024-053). Two cotype specimens are deposited in 1) the collections of the Department of Mineralogy and Petrology, National Museum in Prague, Cirkusová 1740, 19300 Praha 9, Czech Republic, under the catalogue number P1P27/2024 (polished section used for initial WDS analysis to confirm the dominance of Ba over K) and in the Muséum cantonal des sciences naturelles (Naturéum), Département de géologie, Université de Lausanne, Switzerland, under the catalog number MGL 087280 & 087281 (several fragments for final EPMA-WDS, structure determination by 3D ED, powder X-ray diffraction, spectroscopy methods, and optics).

Here, we report on the description of the new mineral, including its crystal-structure determination and refinement from the 3D electron diffraction data.

Occurrence

Barronite was found by one of the authors (CS) on the specimens originating from the Menzenschwand/Krunkelbach uranium deposit, Black Forest Mts. (Schwarzwald), Baden-Würtemberg, Germany (47°50'19.60"N / 8° 2'43.38"E). This locality is a famous occurrence of supergene minerals, in which more than 40 uranium-bearing mineral species have been reported. Barronite is the ninth new mineral to bedescribed from Menzenschwand, the other being metauranocircite (Gaubert, 1904), joliotite (Walenta, 1976), arsenuranospathite (Walenta, 1978), uranosilite (Walenta, 1983), uranotungstite (Walenta, 1985), arsenovanmeersscheite (Walenta and Theye, 2007), nielsbohrite (Walenta *et al.*, 2009) and heisenbergite (Walenta and Theye, 2012). For details on the history of mining, geology and mineralogy of this deposit, see Markl and Wolfsried (2011).

Barronite is of supergene origin; its formation is the result of the oxidation-hydration of uraninite/pitchblende in the supergene zone *in-situ* along with other uranyl silicates and, also most probably, phosphates/arsenates (Göb *et al.*, 2011; Plášil, 2014; Steciuk *et al.*, 2022). The large amount of baryte in the gangue explains the abundance of supergene minerals containing barium. In particular, the Menzenschwand deposit is famous for the abundance of metauranocircite and billietite. Disequilibrium ^{234}U–^{230}Th ages of supergene uranium minerals date the formation to 250–350 Ka (Hofmann and Eikenberg, 1991), whereas the lower intercept of U–Pb dating on metauranocircite gave an age of 1.7 Ma (Pfaff *et al.*, 2009).

Physical and optical properties of barronite

https://doi.org/10.1180/mgm.2025.10081 Published online by Cambridge University Press

Barronite occurs in globular/acicular aggregates consisting of long-prismatic crystals, having maximally 0.3 mm in length, in vugs of gangue dominantly composed of baryte and quartz (Fig. 1). Some of the crystals have a brown-orangish tint, caused by the presence of Fe-Si-gels growing on them. Crystals have a pale yellow colour and colourless pale yellow streak. It is non-fluorescent in SW and LW ultraviolet light. The Mohs hardness is estimated at 1–2 by analogy with weeksite. Barronite is brittle; with perfect prismatic cleavage, distinct on {100}. The fracture is uneven. Optically, barronite is biaxial positive, with α = 1.599(2), β = 1.607(2), γ = 1.617(3) (measured at 589 nm light), 2*V* (meas.) = 86° (based on the extinctions using the spindle-stage), 2*V* (calc.) = 84° (calculated after Wright, 1951). Dispersion is distinct r>v. Pleochroism is distinct in hues of pale-yellow *X*<*Y*<*Z*. Optical orientation is *X* = **b**, *Y* ∧ **a** ~3° in the obtuse angle β.

Chemical composition and density

Electron probe microanalyses (13 points on a homogeneous aggregate of crystals) were performed at the Masaryk University in Brno (Czech Republic) on a Cameca SX-100 electron microprobe operating in WDS mode. Analytical conditions were 15 kV accelerating voltage, 4 nA beam current, and 15 μm beam diameter. Raw X-ray intensities were corrected for matrix effects with a $\phi\rho(z)$ algorithm *X-PHI* (Merlet, 1994). The content of K was corrected for spectral interferences of K*K*α line with U*M*β using an empirical overlap correction. The content of H_2O was not determined directly due to the scarcity of pure material. The H_2O content was calculated based on 1 OH and 2 H_2O was derived from the structure refinement. The crystal structure, infrared and Raman spectroscopy data confirm the presence of OH groups and H_2O and the absence of B–O, C–O and N–O bonds in the mineral. Analytical data are given in Table 1.

The empirical formula (calculated based on 19 O atoms) is $(\square_{1.369}Ba_{0.345}K_{0.165}Ca_{0.086}Pb_{0.024}Fe_{0.011})_{\Sigma 2.000}(U_{0.996}O_2)_2Si_{4.989}O_{12}(OH) \cdot 2H_2O$. The calculated density for the empirical formula (Z = 4) and unit-cell parameters obtained from powder X-ray diffraction data is 3.63 g.cm^{-3}. The ideal formula is: $Ba_{0.5}(UO_2)_2Si_5O_{12}(OH)\cdot 2H_2O$, which requires BaO 7.71, UO_3 57.54$_3$, SiO_2 30.22 and H_2O 4.53, total 100.00 wt.%.

Infrared and Raman spectroscopy

The Attenuated Total Reflectance (ATR) spectra of barronite were recorded by using a micro FTIR LUMOS II spectrometer (Bruker) equipped with a germanium ATR crystal (*n* = 4.0). Spectra were collected in the 450–4000 cm^{-1} range by co-addition of 250 scans with a resolution of 4 cm^{-1} using DLaTGS detector. The spectrum was processed by ATR correction algorithm, in OPUS software, using the mean refractive index of barronite.

The Raman spectra were obtained from loose crystals using a Labram HR Evolution spectrometer. This dispersive, edge-filter-based system is equipped with an Olympus BX 41 optical microscope, a diffraction grating with 600 grooves per millimeter, and a Peltier-cooled, Si-based charge-coupled device (CCD) detector. After careful tests with different lasers (473, 532 and 633 nm), the 532 nm Nd:YAG diode pumped laser with a nominal power of 50 mW attenuated to 10% by neutral density filter was selected for spectra acquisition to minimize analytical artifacts. The Raman signal was collected in the range of 80–4000 cm^{-1} with a 100× objective (NA 0.9) in confocal mode, and beam diameter was ~1 μm and the

https://doi.org/10.1180/mgm.2025.10081 Published online by Cambridge University Press

axial resolution ~2 μm. No visual damage to the analyzed surface was observed at these conditions after the excitation. Wavenumber calibration was done using the Rayleigh line and low-pressure Ne-discharge lamp emissions. The wavenumber accuracy was ~0.5 cm^{-1}, and the spectral resolution was ~2 cm^{-1}. Band fitting was done after appropriate background correction, assuming combined Lorentzian-Gaussian band shapes using the Voigt function.

The ATR corrected IR spectrum is shown in Figure 2a, deconvoluted absorption bands in the IR spectra (Figure 2b,c) and Raman bands (Figure 3a, b) of barronite were assigned as follows: Observed overlapping bands at 3610, 3557, 3502, 3438, and 3266 cm^{-1} (IR) and 3613, 3557, 3459 and 3226 cm^{-1} (Raman) corresponds to O−H stretching vibrations. According to the empirical relation between the energy of vibration and the corresponding bond length (Libowitzky, 1999), O-H···O (H···*Acceptor*) bond lengths vary approximately in the range from 1.85 to 2.4 Å. The broad band at 3003 cm^{-1} (IR) and several overlapping bands at 2992–2852 cm^{-1} (Raman) could be attributed to the stretching mode of SiO_3O−H. Similar vibrations were observed in haiweeite (Frost *et al.*, 2006). The vibrations at 1645 and 1629 cm^{-1} (IR) and 1639 cm^{-1} (Raman) correspond to the H_2O bending mode. The IR band at 1437 cm^{-1} and Raman bands at 1165, 1133 and 1009 cm^{-1} are attributed to Si-OH bending modes of SiO_3OH (Čejka 1999; Frost *et al.*, 2006; Colmenero *et al.*, 2019), and a band at 938 cm^{-1} corresponds to antisymmetric stretching vibrations of SiO_4 groups. These bands are also visible in IR spectrum at 1206, 1179, 1147, 1108, 1060 and 994 cm^{-1}. The bands at 917 and 870 (IR) correspond to the split triply degenerated ν_3 antisymmetric stretching vibrations of UO_2, and a prominent Raman band at 808 cm^{-1} and probably some shoulders (Raman) are attributed to ν_1 symmetric stretching vibrations of UO_2, partially overlapping symmetric stretching vibrations of SiO_4 at 750–600 cm^{-1} (IR) and ~750 cm^{-1} (Raman). Using the empirical relationship of Bartlett and Cooney (1989) between vibration energies of ν_3 $(UO_2)^{2+}$ and ν_1 $(UO_2)^{2+}$ and the corresponding U–O bond lengths, we have calculated the approximate U–O bond lengths as follows (in Å): 1.77 (from 917 cm^{-1}), 1.81 (870 cm^{-1}) and 1.80 (808 cm^{-1}). These values are in line with the structure refinement. The region between 600–500 cm^{-1} comprises bending modes of SiO_4 and water libration modes, whereas bending modes of UO_2 are tentatively assigned to the Raman band at 265 cm^{-1}, by analogy with weeksite (Frost *et al.*, 2006).

Crystallography and crystal structure of barronite

X-ray powder diffraction data

Powder X-ray diffraction data were collected at room temperature using a PANalytical Empyrean diffractometer (λ = 1.54184 Å) equipped with a focusing Göbel mirror (producing high-intensity Cu$K\alpha_{1,2}$ beam), capillary holder, and solid-state PIXcel^{3D} detector. The instrument was operating at 45 kV and 40 mA. Barronite crystals were crushed mildly in acetone and loaded into a 0.3 mm capillary. The powder data were collected in the Debye-Scherrer geometry in the range 3–90° 2θ, integrated step 0.015° and a counting time of 50 s per step (total experiment duration was ca. 72 hours). Visual inspection follwing data collection found no evidence of sample dehydration or damage. Positions and intensities of diffractions were found and refined using the Pearson VII profile-shape function of the ZDS

https://doi.org/10.1180/mgm.2025.10081 Published online by Cambridge University Press

program package (Ondruš, 1993). The unit-cell parameters of barronite were refined by the least-squares program of Burnham (1962). The X-ray powder diffraction data of barronite are provided in Table 2. The refined unit-cell parameters (298 K) (for the space group *C*2/*m*) are *a* = 14.1955(13) Å, *b* = 14.1904(8) Å, *c* = 9.6296(8) Å, β = 111.634(5)°, with *V* = 1803.1(3) Å^3 (*Z* = 4). The refined unit cell volume obtained from the data collected at the 298 K is slightly larger than that obtained from the 3D ED at 95K (1788.2 Å^3) and is actually close to the one of the natural weeskite (~1808 Å^3; Fejfarová *et al.*, 2012.

Single crystal 3D electron diffraction

Because barronite crystals are thin, long, relatively small and intergrown in parallell aggregates (Fig. 4a), no useful single-crystal X-ray data could be acquired. Therefore, the 3-dimensional electron diffraction techniques (3D ED) were used (Gemmi and Lanza, 2019; Gemmi *et al.*, 2019). Aggregates of barronite crystals were gently crushed in acetone and deposited on a Cu-grid coated by a thin film of holey amorphous carbon. 3D ED data were collected with a FEI Tecnai G2 20 transmission electron microscope (TEM) (acceleration voltage of 200 kV, LaB_6) equipped with a side-mounted hybrid single-electron detector ASI Cheetah M3, 512 × 512 pixels with high sensitivity and a fast readout. To preserve the hydrated structure of the mineral under the high vacuum in the TEM, the grid was plunged into liquid nitrogen and transferred to the TEM using a Gatan cryo-transfer holder. The PEDT (precession electron diffraction tomography) technique was chosen to reduce the dynamical effects further, using the precession device Nanomegas Digistar (Vincent and Midgley, 1994) and a precession semi-angle of 1°. Data sets were all collected at 94 K on several single crystals in stepwise mode with a tilt step of the goniometer set to 1° on the accessible tilt range allowed by the preparation (Fig. 4a). To limit the beam-induced damage to the crystals, low illumination settings were used. 3D ED data reduction was performed using the computer program PETS2 (Palatinus *et al.*, 2019; Brázda *et al.*, 2022; Khouchen *et al.*, 2023). The structure analysis was performed from the best data set, associated with the lowest Rocking curve width and apparent mosaicity of the crystal (Fig. 4b). For each 3D ED data set, the data reduction yielded two *hkl*-type files. The first one assumes the kinematical approximation (for structure solution and the so-called kinematical refinement) with R_{int}(obs/all) = 0.1362/0.1451and 76 % coverage for $\sin\theta_{max}/\lambda$ = 0.8Å^{-1} (Laue class *mmm*). The second was for the dynamical refinement in which all frames of the data set were independently refined. The data coverage was limited due to the strong preferential orientation on the grid along [010]. The structure was solved assuming the kinematical approximation using Superflip (Palatinus and Chapuis, 2007; Palatinus, 2013) implemented in Jana2020 (Petříček *et al.*, 2023). The refinement considering the dynamical theory of diffraction was carried out through DYNGO and Jana2020 (Palatinus *et al.*, 2015a, b). Based on the 3D ED data, the following monoclinic unit cell (at 94K) was obtained: *a* = 14.2115(11) Å, *b* = 14.0169(19) Å, *c* = 9.6545(8) Å, *β* = 111.59(6)°, with *V* = 1788.2(8) Å^3 (*Z* = 4). A projection of the reciprocal space along [010] shows a two-fold axis twinning along (104), as it was observed in the related structure of weeksite (Fejfarová *et al.*, 2012) (Fig. 5a). It is a typical example of twinning due to reticular merohedry (diffraction type II; Petříček *et al.*, 2016). Sections through the reciprocal space indicated the space group *C*2/*m*, later confirmed by the structure

analysis (Fig. 5b). The high quality of the 3D ED data collected on barronite is represented on the Rocking curve plot profile (Fig. 4b) with a sharply observed profile (blue on Fig. 4b), very low values for the *Rocking curve width* = 0.0011 $Å^{-1}$ and the *apparent mosaicity* = 0.038°, and high-angular resolution data. The structure was solved *ab initio* from a data set with 76% completeness up to the resolution of $\sin(\theta_{max})/\lambda = 0.8$ $Å^{-1}$. The completeness is limited due to the [010] preferred orientation of the crystals on the grid and the incomplete rotation of the goniometer. The model was then refined using the dynamical theory of electron diffraction, which is necessary to reach fine structural details from 3D ED data. The two cationic sites in the cavity formed by the uranyl and silicon framework are assumed to be occupied by a mixture of Ba, Ca and K with a ratio set according to the chemical analysis. The overall occupancies of the two sites were refined with set ratios between cations. Partially occupied oxygen sites (OH and H_2O) were added to the cavity during the refinement. The dynamical refinement converged towards R(obs)/wR(obs) = 0.0791/0.0811, R(all)/wR(all) = 0.1380/0.0864 for 6596/15684 observed/all reflections and 193 refined parameters. Those values are very satisfying for electron diffraction data collected on inorganic material with heavy atoms and twinning present. Additional details about the parameters used in the refinement are given in Table 3. The distribution of (OH) and H_2O over the O sites was deduced from the bond valence analysis. At this stage of development, the dynamical refinement of twinned 3D ED data still represents a challenge despite the data's very high quality and resolution. In this work, it does not affect the model much. However, the Fourier difference map (difference electrostatic potential map) remains uncertain, explaining why H atom positions could not be resolved. Positional parameters are presented in Table 4, interatomic distances in Table 5, and the bond-valence analysis in Table 6. Barronite structure is shown in Figures 6 and 7. The structure obtained from 3D ED is provided as a CIF file and was deposited in the CCDC database under the deposition number 2417188.

Description of the barronite crystal structure

In the structure of barronite, there are one U site, three Si sites, two M sites (occupied dominantly by Ba, less by K and Ca), and thirteen O sites; of the O sites, one is $(OH)^-$ and four are H_2O. The U atom is strongly bonded (at ~1.8 Å) to two O atoms (O1, O5), forming a uranyl ion, $(UO_2)^{2+}$. This moiety is further coordinated by five O ligands in the equatorial plane, thus forming a uranyl pentagonal bipyramid (*UPB*) (Table 5); this is the most frequent coordination of hexavalent uranium in the solid state (Lussier *et al.*, 2016). *UPB*s share equatorial edges to form chains parallel to [100], which share edges with $(Si1)O_4$ tetrahedra. The remaining ("free") vertex of the uranyl pentagonal bipyramid is then linked to a $(Si2)O_4$ tetrahedron. The uranyl silicate chains are linked to crankshaft-like chains of vertex-sharing SiO_4 tetrahedra, resulting in layers connected through vertex-sharing between $Si(3)O_3(OH)$ tetrahedra to form an open framework. In the channels of this framework structure, two independent *M* sites are occupied dominantly by divalent (Ba^{2+}, Ca^{2+}) and monovalent cations (K^+). Three O sites hosted by H_2O (based on bond-valence analysis, Table 6) are bonded to *M* sites, whereas one is only weakly bonded in the channels. The two most important differences between the barronite and weeksite structure are that, inbarronite (1) the dominant cation in the channels is Ba^{2+} and (2) a shared vertex between two neighboring (symmetrically related)

https://doi.org/10.1180/mgm.2025.10081 Published online by Cambridge University Press

Si3 tetrahedra is protonated, forming a SiO_3OH group. The protonation of the silicate tetrahedron is apparent from the bond-valence analysis (Table 6). The structural formula obtained from the results of the refinement and the bond-valence considerations is $(Ba_{0.41}K_{0.22}Ca_{0.08})_{\Sigma 0.71}{}^{\Sigma charge\,=\,1.2+}(UO_2)_2Si_5O_{12}(OH)\cdot 1.96H_2O$ (Z = 4). This formula is has a 0.2 charges excess; however, note thatthe cation content in the Ba sites can suffer from a small inaccuracy due to the twinned data, the multiple substitutions on the Ba sites, and possible nano compositional variations as compared with the microprobe analysis. Moreover, the O↔OH substitution at $O2_{Si3}$ (Table 6) provides another charge-balancing mechanism. Molecular water content might also be somewhat variable, depending on the amount of metal cations distributed over the sites in the channels.

Structural complexity of barronite

The structural complexity of barronite was determined as the Shannon information content per atom (I_G) and per unit cell ($I_{G,total}$). This approach was developed by Krivovichev (2012, 2013, 2014, 2016, 2017): the complexity of a crystal structure can be quantitatively characterized by the amount of Shannon information, which is measured in bits (binary digits) per atom (bits/atom) and per unit cell (bits/cell), respectively. The concept of Shannon information, also known as Shannon entropy, used herein originates from information theory. The amount of Shannon information reflects the diversity and relative proportion of different objects, e.g., the number and relative proportion of different sites in an elementary unit cell of a crystal structure. The information-based structural complexity values were calculated using the software package TOPOS (Blatov *et al.*, 2014). The chemical complexity (after Siidra *et al.*, 2014) is estimated by considering the chemical formula as a message, where symbols correspond to different chemical elements.

Calculated values for the structural complexity of barronite in comparison with other uranyl silicate minerals are reported in Table 8. Barronite, with a complexity of 410.4 bits/unit-cell, belongs to the intermediate-complex structures (following the classification of Krivovichev, 2013), and is very similar in those measures to then structurally similar weeksite, but it is of a smaller magnitude due to the lower H_2O content in barronite.

Discussion

The content of molecular water in the weeksite-type structures

Based on the results of the crystal structure refinement from 3D ED data, barronite contains ~2 H_2O (1.965) in the channels of its microporous structure. It is straightforward to compare this value with previous results of the structure studies on both natural weeksite (Fejfarová *et al.*, 2012) and synthetic analogs (Nazarchuk *et al.*, 2025). Natural weeskite specimen studied by Fejfarová *et al.* (2012) provided enough pure material that allowed the employment of a thermogravimetric study. The observed mass loss up to ~660°C was approximately 6.7 wt.% which corresponds quite well with the content of 4 H_2O in the structure of natural weeksite. Recently, Nazarchuk *et al.* (2025) reported on new structure data for natural weeksite, its synthetic counterpart (K-dominant) and isotypic Rb- and Cs-dominant synthetic phases. Unfortunately, the direct determination of the H_2O content was not possible. We can comment on the values obtained from the crystal structure refinements only. The refinements of all phases were affected by the nature and behavior of the H_2O in

https://doi.org/10.1180/mgm.2025.10081 Published online by Cambridge University Press

weeksite-type channels. It is, up to a significant extent, "zeolitic". The H_2O content in the synthetic weeksite was deduced to be less than observed in the natural weeksite, of about 2.5 H_2O. In Rb and Cs analogs, they inferred content of 2.34 and 2.20 H_2O *apfu*, which is in line with the presence of cations with larger ionic radii than K: $^{[8]}$Rb+ = 1.667 Å, $^{[8]}$Cs+ = 1.878 Å vs. $^{[8]}$K= 1.495 Å (Hawthorne and Gagné, 2024). From the point of view of a clear relationship between the size of the cations hosted within cavities and decreasing H_2O content while keeping the size of the channels/cavities unchanged (or to a lower extent), the H_2O content found by the current study in barronite, is striking. Divalent barium is much smaller ([7] = 1.427 Å and [8] = 1.450 Å) than Rb and Cs and one would await a higher amount of H_2O bonded in the structure. The unit-cell volume obtained for barronite at 298 K is very similar to those of natural weeksite. The volume obtained at the low temperatures from the 3D ED data, ~1788 $Å^3$, is much more convincing for the presence of much smaller cations in the channels. If it is just a relic of the methodology (TEM analysis in the high vacuum under the electron beam and the real water content of H_2O in barronite is somewhat higher, or if it is caused by something else, we cannot reliably decide without further studies.

The presence of Ba^{2+} atoms in the weeksite-type structures – implications

Barronite is the first known mineral, or synthetic phase, of weeksite-type structures that contains divalent cations of alkaline earth metals. Previous studies on weeksite (Jackson and Burns, 2001; Fejfarová *et al.*, 2012) have reported that it can contain certain amounts of barium, with up to 3.7 wt.% BaO. Weeksite-type structures are also likely capable of hosting strontium, which has a smaller ionic radius compared to barium in the currently investigated structure of barronite. According to Hawthorne and Gagné (2024), the ionic radius of Sr^{2+} is [7] = 1.273 Å and [8] = 1.292 Å, while for Ba^{2+} it is [7] = 1.427 Å and [8] = 1.450 Å. Additionally, potassium, which is primarily found in weeksite (Fejfarová *et al.*, 2012), has an ionic radius of [7] = 1.495 Å and [8] = 1.528 Å. We conclude that microporous framework structures of the weeksite type could be effective for immobilizing the fission product radionuclide strontium-90 (^{90}Sr). This particular isotope is significant within spent nuclear fuel due to its high activity, though it has a relatively short half-life of about 30 years (Ewing, 2015), making it less relevant for long-term nuclear fuel storage. However, barronite and weeksite-type phases may still be important when considering the possible interactions between nuclear fuel and water solutions that contain dissolved silicon in the early stages of the temporary disposal.

Acknowledgements. The helpful and constructive edits of Anthony Kampf, Oleg Siidra and Peter Leverettare greatly appreciated. This study was supported by the CzechNanoLab Research Infrastructure supported by MEYS CR (LM2023051) (JP). Additionally, we acknowledge the support by the Ministry of Culture of the Czech Republic (long-term project DKRVO 2024-2028/1.II.b; National Museum, 00023272) for JS and ZD and OP VVV project (Geobarr CZ.02.1.01/0.0/0.0/16_026/0008459) to RS.

Competing interests. The authors declare none.

Supplementary material. The supplementary material for this article can be found at .....

References

Bartlett J.R. and Cooney R.P. (1989) On the determination of uranium-oxygen bond lengths in dioxouranium(VI) compounds by Raman spectroscopy. *Journal of Molecular Structure*, **193**, 295–300.

Blatov, V.A., Shevchenko, A.P. and Proserpio, D.M. (2014) Applied topological analysis of crystal structures with the program package ToposPro. *Crystal Growth &Design*, **14**, 3576–3586.

Brázda P., Klementová, M., Krysiak, Y. and Palatinus, L. (2022) Accurate lattice parameters from 3D electron diffraction data. I. Optical distortions. *International Union of Crystallography Journal*, **9**, 1–21.

Brown, I.D. (2002) The chemical bond in inorganic chemistry: the bond valence model. Oxford University Press, UK, 1–278.

Burnham C. W. (1962) Lattice constant refinement. *Carnegie Institute Washington Yearbook*, **61**, 132–135.

Burns, P.C. (1998) The structure of boltwoodite and implications of solid solution toward sodium boltwoodite. *The Canadian Mineralogist*, **36**, 1069–1075.

Colmenero, F., Plášil, J. and Sejkora, J. (2019). The layered uranyl silicate mineral uranophane-β: Crystal structure, mechanical properties, Raman spectrum and comparison with the α-polymorph. *Dalton Transactions*, **48**, 167220–16736.

Čejka, J. (1999). Infrared spectroscopy and thermal analysis of the uranyl minerals. Reviews in Mineralogy and Geochemistry, 38(1), 521-622.

Demartin, F., Gramaccioli, C. M. and Pilati, T. (1992) The importance of accurate crystal structure determination of uranium minerals. II. Soddyite $(UO_2)_2(SiO_4)\cdot 2H_2O$. *Acta Crystallographica*, **C48**, 1–4.

Ewing, R.C. (2015) Long-term storage of spent nuclear fuel. *Nature Materials*, **14**, 252–257.

Fejfarová, K., Plášil, J., Yang, H., Čejka, J., Dušek, M., Downs, R. T., Barkley, M. C., and Škoda, R. (2012) Revision of the crystal structure and chemical formula of weeksite, $K_2(UO_2)_2(Si_5O_{13})\cdot 4H_2O$. *American Mineralogist*, **97**, 750–754.

Fejfarová, K., Dušek, M., Plášil, J., Čejka, J., Sejkora, J., and Škoda, R (2013) Reinvestigation of the crystal structure of kasolite, $Pb[(UO_2)(SiO_4)](H_2O)$, an important alteration product of uraninite, UO_{2+x}. *Journal of Nuclear Materials*, **434** (1) 461–467.

Frost R. L., Čejka J., Weier M. L., Martens W. and Kloprogge J. T. (2006) A Raman and infrared spectroscopic study of the uranyl silicates-weeksite, soddyite and haiweeite. *Spectrochimica Acta A*, **64**, 308–315.

Gagné O. and Hawthorne F.C. (2015) Comprehensive derivation of bond-valence parameters for ion pairs involving oxygen. *Acta Crystallographica*, **B71**, 562–578.

Gaubert, P. (1904) Produits deshydration de quelque phosphates et orientation du chlorure de baryum sur les mineraux des groups de l'autunite. *Bulletin de la Société Française de Minéralogie*, **27**, 212–216.

Gemmi M. and Lanza A.E. (2019) 3D electron diffraction techniques. *Acta Crystallographica Section B: Structural Science, Crystal Engineering and Materials*, **75**, 495–504.

Gemmi M., Mugnaioli E., Gorelik T.E., Kolb U., Palatinus L., Boullay P., Hovmöller S. and Abrahams J.P. (2019) 3D electron diffraction: The nanocrystallography revolution. *ACS Central Science*, **5**, 1315–1329.

https://doi.org/10.1180/mgm.2025.10081 Published online by Cambridge University Press

Ginderow, D. (1988) Structure de l´uranophane alpha, $Ca(UO_2)_2(SiO_3OH)_2 \cdot 5H_2O$. *Acta Crystallographica*, **C44**, 421–424.

Göb, S., Wenzel, T., Bau, M., Jacob, D.E., Loges, A., and Markl, G. (2011) The redistribution of rare-earth elements in secondary minerals of hydrothermal veins, Schwarzwald, southwestern Germany. *Canadian Mineralogist*, **49**, 1305–1333.

Hawthorne, F.C., and Gagné, O.C. (2024) New ion radii for oxides and oxysalts, fluorides, chlorides and nitrides. *Acta Cryst.*, **B80**, 326–339.

Hofmann, B. and Eikenberg, J. (1991) The Krunkelbach Uranium deposit, Schwarzwald, Germany: Correlation of radiometric ages (U-Pb, U-Xe-Kr, K-Ar, ^{230}Th-^{234}U) with mineralogical stages and fluid inclusions. *Economic Geology*, **86**, 1031–1049.

Jackson, J. M. and Burns, P. C. (2001) A re-evaluation of the structure of weeksite, a uranyl silicate framework mineral. *The Canadian Mineralogist*, **39**, 187–195.

Khouchen M., Klar P.B., Chintakindi H., Suresh A. and Palatinus L. (2023) Optimal estimated standard uncertainties of reflection intensities for kinematical refinement from 3D electron diffraction data. *Acta Crystallographica*, **A79**, 427–439.

Kraus, W. and Nolze, G. (1996) POWDER CELL – a program for the representation and manipulation of crystal structures and calculation of the resulting X-ray powder patterns. *Journal of Applied Crystallography*, **29**, 301–303.

Krivovichev, S.V. (2012) Topological complexity of crystal structures: quantitative approach. *Acta Crystallographica*, **A68**, 393–398.

Krivovichev, S.V. (2013) Structural complexity of minerals: information storage and processing in the mineral world. *Mineralogical Magazine*, **77**, 275–326.

Krivovichev, S.V. (2014) Which inorganic structures are the most complex? *Angewandte Chemistry, International Edition*, **53**, 654–661.

Krivovichev, S.V. (2016) Structural complexity and configurational entropy of crystals. *Acta Crystallographica*, **B72**: 274–276.

Krivovichev, S.V. (2017) Hydrogen bonding and structural complexity of the $Cu_3(AsO_4)(OH)_3$ polymorphs (clinoclase, gilmarite): a theoretical study. *Journal of Geosciences*, **62**, 79–85.

Kubatko, K.A., and Burns, P.C. (2006) A novel arrangement of silicate tetrahedra in the uranyl silicate sheet of oursinite, $(Co_{0.8}Mg_{0.2})[(UO_2)(SiO_3OH)]_2(H_2O)_6$. *American Mineralogist*, **91**, 333–336.

Libowitzky E. (1999) Correlation of O-H stretching frequencies and O-H···O hydrogen bond lengths in minerals. *Monatshefte für Chemie*, **130**, 1047–1059.

Lussier A.J., Lopez R.A. and Burns P.C. (2016) A revised and expanded structure hierarchy of natural and synthetic hexavalent uranium compounds. *The Canadian Mineralogist*, **54**, 177–283.

Markl, G., and Wolfsried, S. (2011) Das Uran von Menzenschwand. Chr. Weise Verlag, Munich, 143 pages.

Merlet, C. (1994) An Accurate Computer Correction Program for Quantitative Electron Probe Microanalysis. *Microchimica Acta*, **114/115**, 363–376.

Nazarchuk, E.V., Tagirova, Y.G., Siidra, O., Charkin, D.O., Dmitriev, D.N., Kalmykov, S.N., Kasatkin, A.V., and Plášil, J. (2025) Polythermal studies of weeksite, a microporous uranyl silicate, and its synthetic analogues. *Mineralogical Magazine, under review.*

https://doi.org/10.1180/mgm.2025.10081 Published online by Cambridge University Press

Ondruš P. (1993) A computer program for analysis of X-ray powder diffraction patterns. *Materials Science Forum, EPDIC-2, Enchede,* 133-136, 297-300.

Palatinus L. (2013) The charge-flipping algorithm in crystallography. *Acta Crystallographica,* **B69**, 1–16.

Palatinus L. and Chapuis G. (2007) SUPERFLIP—a computer program for the solution of crystal structures by charge flipping in arbitrary dimensions. *Journal of Applied Crystallography*, **40**, 786–790.

Palatinus L., Corrêa C.A., Steciuk G., Jacob D., Roussel P., Boullay P., Klementová M., Gemmi M., Kopeček J., Domeneghetti M.C., Cámara, F. and Prtříček, V. (2015a) Structure refinement using precession electron diffraction tomography and dynamical diffraction: tests on experimental data. *Acta Crystallographica,* **B71**, 740–751.

Palatinus L., Petříček V. and Correâ C.A. (2015b) Structure refinement using precession electron diffraction tomography and dynamical diffraction: Theory and implementation. *Acta Crystallographica,* **A71**, 235–244.

Palatinus L., Brázda P., Jelínek M., Hrdá J., Steciuk G., and Klementová M. (2019) Specifics of the data processing of precession electron diffraction tomography data and their implementation in the program PETS2.0. *Acta Crystallographica*, **B75**, 512–522.

Petříček, V., Dušek, M. and Plášil, J. (2016) Crystallographic computing system Jana2006: Solution and refinement of twinned structures. *Zeitschrift für Kristallographie*, **231**, 583–599.

Petříček V., Palatinus L., Plášil J. and Dušek M. (2023) Jana2020 - a new version of the crystallographic computing system Jana. *Zeitschrift für Kristallographie*, **238**, 271–282.

Pfaff, K., Romer, R.L., and Markl, G. (2009) U-Pb ages of ferberite, chalcedony, agate, 'U-mica' and pitchblende: constraints on the mineralization history of the Schwarzwald ore district. *European Journal of Mineralogy*, **21**, 817–836.

Plášil, J. (2014) Oxidation–hydration weathering of uraninite: the current state-of-knowledge. *Journal of Geosciences*, **59**, 99–114.

Plášil, J., Fejfarová, K., Čejka, J., Dušek, M., Škoda, R., and Sejkora, J. (2013) Revision of the crystal structure and chemical formula of haiweeite, $Ca(UO_2)_2(Si_5O_{12})(OH)_2{\cdot}6H_2O$. *American Mineralogist*, **98**, 718–723.

Plášil, J., Petříček, V., Locock, A.J., Škoda, R., and Burns, P.C. (2018) The (3+3) commensurately modulated structure of the uranyl silicate mineral swamboite-(Nd), $Nd_{0.333}[(UO_2)(SiO_3OH)](H_2O)_{2.41}$. *Zeitschrift für Kristallographie*, **233**, 223–231.

Plášil, J., Steciuk, G., Sejkora, J., Kampf, A.R., Uher, P., Ondrejka, M., Škoda R., Dolníček, Z., Philippo, S., Guennou, M., Meisser, N., Rohlíček, J., and Mees, F. (2025) Extending the mineralogy of U^{6+} (I.): Crystal structure of lepersonnite-(Gd) and a description of the new mineral lepersonnite-(Nd). *Mineralogical Magazine (under review*).

Rosenzweig, A., and Ryan, R.R. (1975) Refinement of the crystal structure of cuprosklodowskite $Cu[(UO_2)_2(SiO_3OH)_2]{\cdot}6H_2O$. *American Mineralogist*, **60**, 448–453.

Ryan, R.R., and Rosenzweig, A. (1977) Sklodowskite, $MgO{\cdot}2UO_3{\cdot}2SiO_2{\cdot}7H_2O$. *Crystal Structure Communications*, **6**, 611–615.

Siidra, O., Zenko, D.S. and Krivovichev, S.V. (2014) Structural complexity of lead silicates: crystal structure of $Pb_{21}[Si_7O_{22}]_2[Si_4O_{13}]$ and its comparison to hyttsjöite. *American Mineralogist*, **99**, 817–823.

https://doi.org/10.1180/mgm.2025.10081 Published online by Cambridge University Press

Steciuk, G., Škoda, R., Dillingerová, V., and Plášil, J. (2022) Chemical variability in vyacheslavite, U $(PO_4)(OH)$: Crystal-chemical implications for hydrous and hydroxylated U^{4+}, Ca, and REE phosphates. *American Mineralogist*, **107**, 131–137.

Vincent R. and Midgley P.A. (1994) Double conical beam-rocking system for measurement of integrated electron diffraction intensities. *Ultramicroscopy*, **53**, 271–282.

Viswanathan, K., and Harneit, O. (1986) Refined crystal structure of β-uranophane $Ca(UO_2)_2(SiO_3OH)_2.5H_2O$. *American Mineralogist*, **71**, 1489–1493.

Walenta, K. (1976) Widenmannit und Joliotit, zwei neue Uranylkarbonatmineralien aus dem Schwarzwald. *Schweizerische Mineralogische und Petrographische Mitteilungen*, **56**, 167–185.

Walenta, K. (1978) Uranospathite and arsenuranospathite. *Mineralogical Magazine*, **42**, 117–128.

Walenta, K. (1983) Uranosilite, ein neues Mineral aus der Uranlagerstätte von Menzenschwand im südlichen Schwarzwald. *Neues Jahrbuch für Mineralogie, Monatshefte*, **1983**, 259–269.

Walenta, K. (1985) Uranotungstit, ein neues sekundäres Uranmineral aus dem Schwarzwald. *Tschermaks Mineralogische und Petrographische Mitteilungen*, **34**, 25–34.

Walenta, K., and Theye, T. (2007) Arsenovanmeersscheit, ein neues Uranmineral von der Uranlagerstätte Menzenschwand im südlichen Schwarzwald. *Aufschluss*, **58**, 159–164.

Walenta, K. and Theye, T. (2012) Heisenbergite, a new uranium mineral from the uranium deposit of Menzenschwand in the Southern Black Forest, Germany. *Neues Jahrbuch für Mineralogie - Abhandlungen*, **189**(2), 117-123.

Walenta, K., Hatert, F., Theye, T., Lissner, F., and Roeller, K. (2009) Nielsbohrite, a new potassium uranyl arsenate from the uranium deposit of Menzenschwand in the Southern Black Forest, Germany. *European Journal of Mineralogy*, **21**, 515–520.

Wright, F.E. (1951) Computation of the optic axial angle from the three principal refractive indices. *American Mineralogist*, **36**, 543–556.

https://doi.org/10.1180/mgm.2025.10081 Published online by Cambridge University Press

FIGURE CAPTIONS

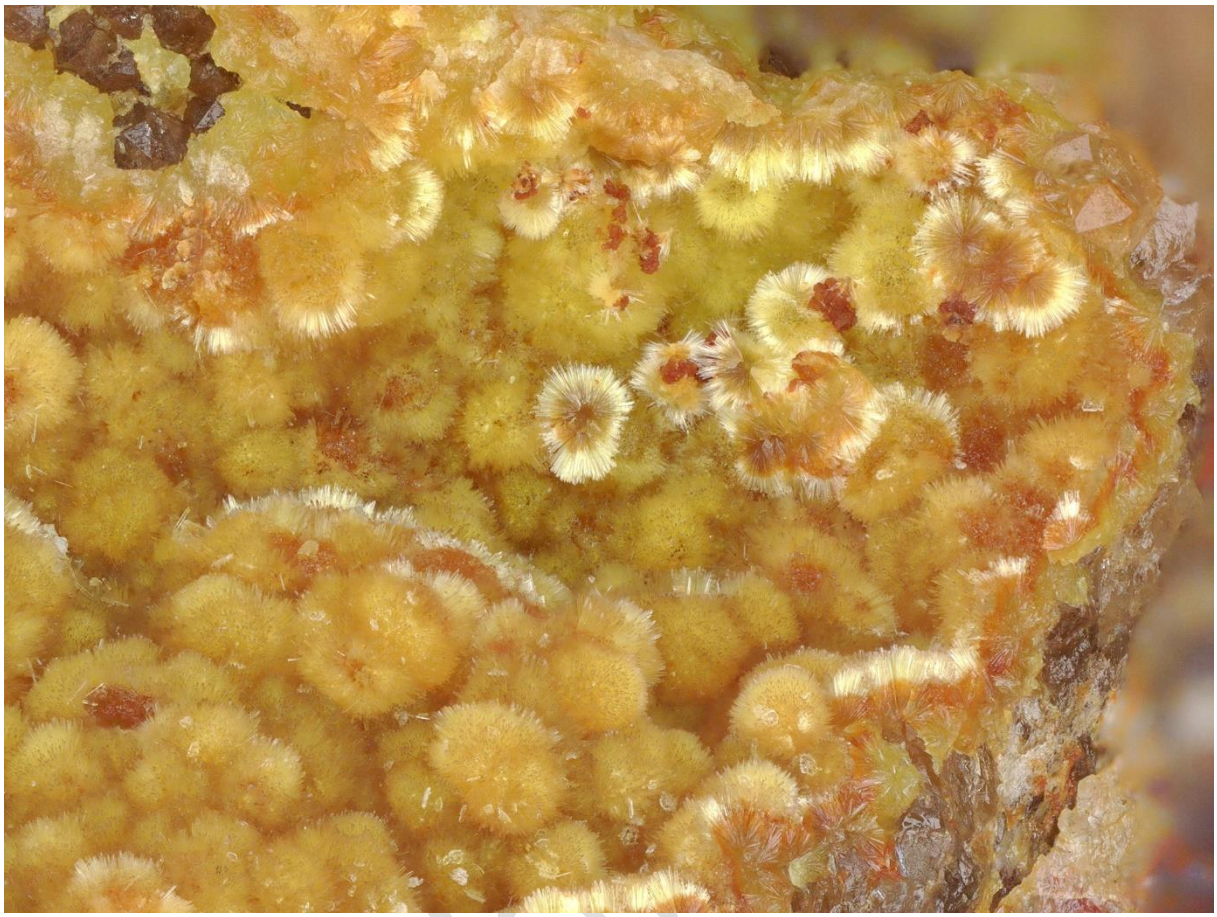

Figure 1. Needle-like crystals of barronite that are forming acicular aggregates in the vug of quartz-barite gangue. Specimen MGL 087281, FOV 2.95 mm (photo by Carsten Slotta).

https://doi.org/10.1180/mgm.2025.10081 Published online by Cambridge University Press

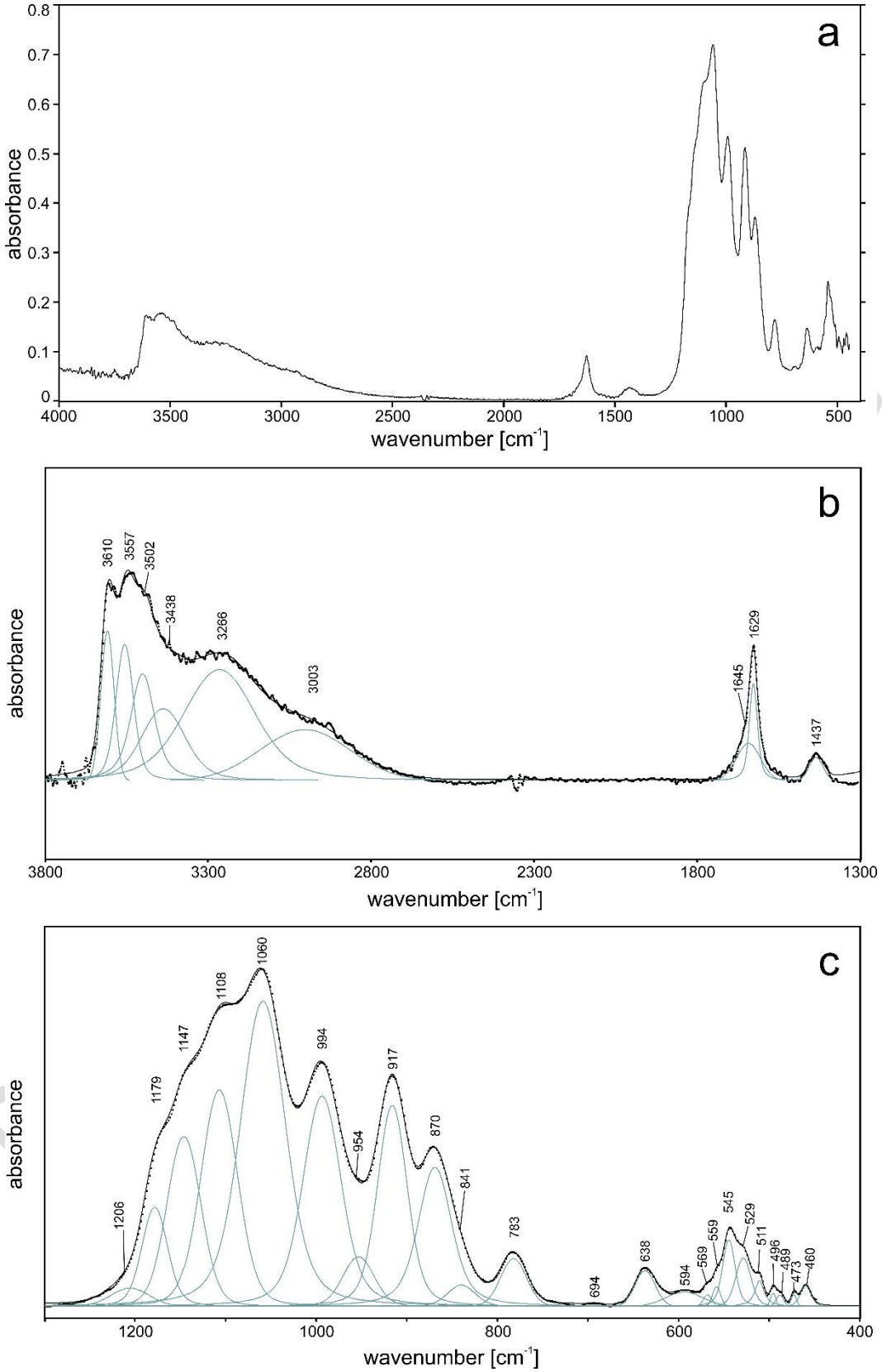

Figure 2. ATR-corrected FTIR spectrum of barronite. **(A)** - entire collected spectrum, **(b)**-spectral fit in the range 3800–1300 cm^{-1}, **(c)**-spectral fit in the range 1300–400 cm^{-1}. For (b, c), the measured spectrum is shown by dots. The black curve matching to dots is a result of spectral fit as a sum of individual Voigt peaks shown below the curve.

https://doi.org/10.1180/mgm.2025.10081 Published online by Cambridge University Press

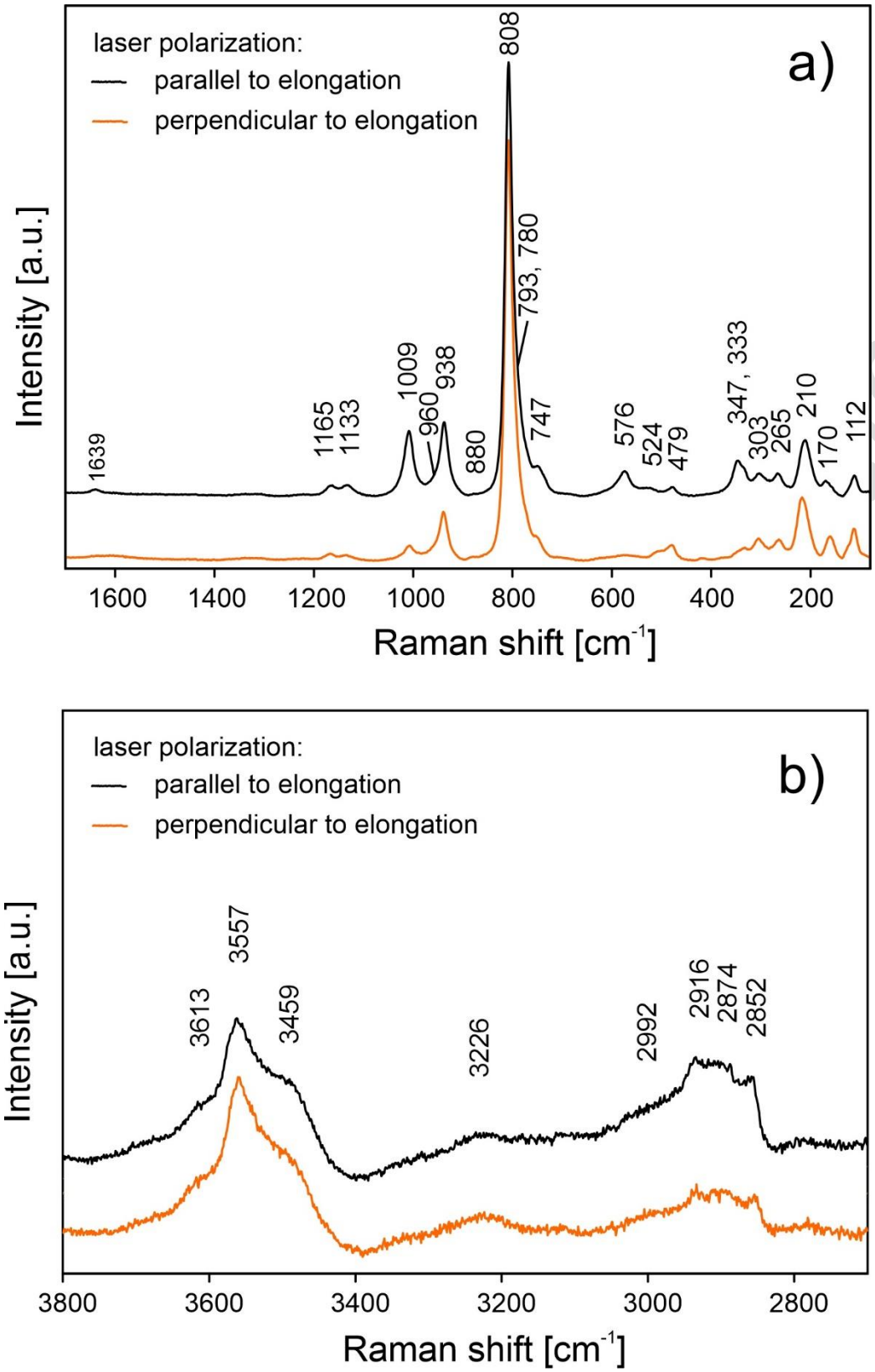

Figure 3. Raman spectra of barronite collected in two perpendicular crystal orientations shown in a**)** 1700–80 cm^{-1} region and **b)** 3800–2700 cm^{-1} region.

https://doi.org/10.1180/mgm.2025.10081 Published online by Cambridge University Press

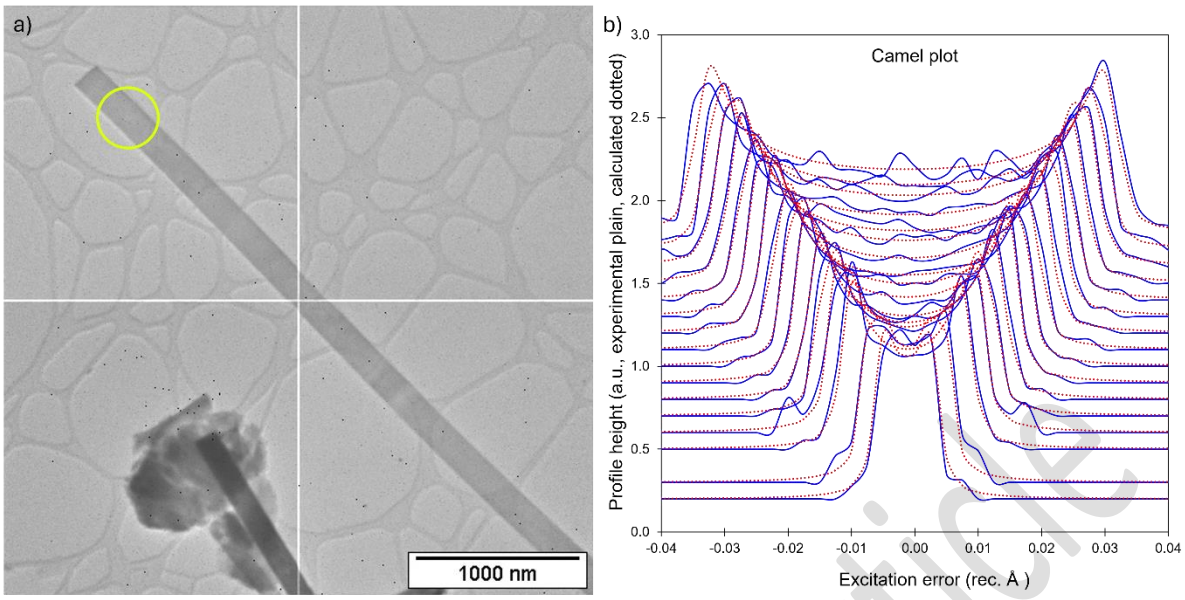

Figure 4. a) Needle-like single crystal of barronite selected for structure characterization. The green circle represents the nanobeam size of about 370 nm for collecting 3DED data. **b)** Plots of the rocking-curve profiles (Camel plot) of the experimental 3D ED data at 94K. The lowest blue curve is the averaged observed rocking curve in the range of 0.2 to 0.3 $Å^{-1}$ and the next ones are obtained by steps of 0.1 $Å^{-1}$. The red curves are the calculated ones from the *Rocking curve width* = 0.0011 $Å^{-1}$, *apparent mosaicity* = 0.0382 °, and precession *semi-angle* = 1 °. Reflections are involved in the Camel plot for $I > 10*\sigma(I)$.

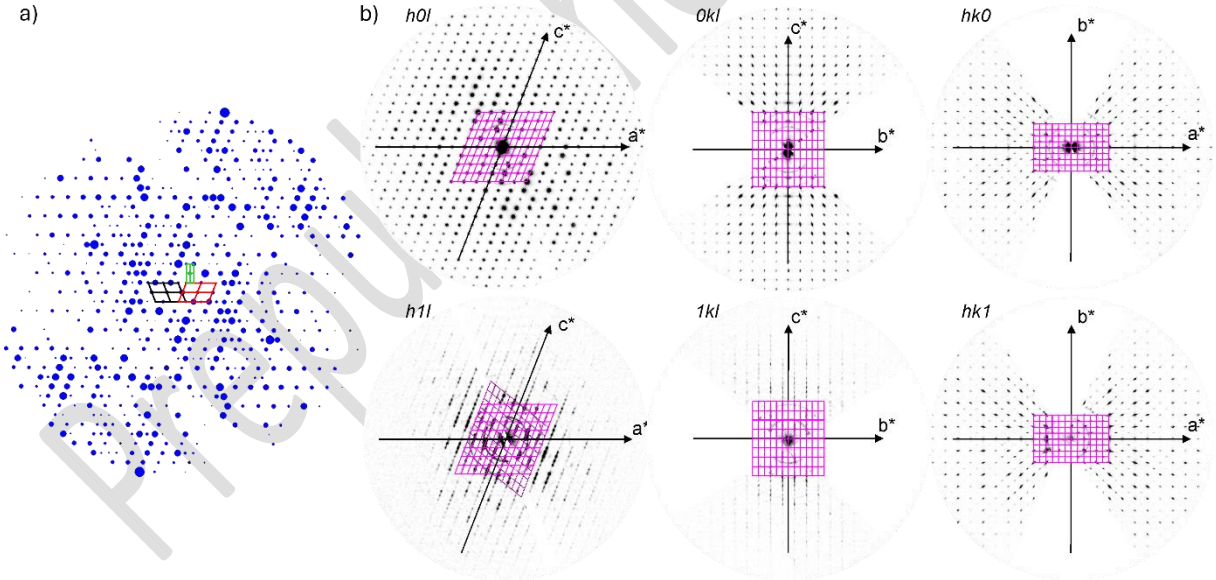

Figure 5 Reciprocal space sections reconstructed from 3D ED data collected on a barronite single-crystal at 94 K. **A)** the outline of the unit cells of barronite (red and black = monoclinic cells related by twinning; green = orthorhombic super-cell); the size of the spots (diffractions) is related to their observed intensities obtained from 3D ED. **B)** precession-like reconstructions of different *hkl*-slices.

https://doi.org/10.1180/mgm.2025.10081 Published online by Cambridge University Press

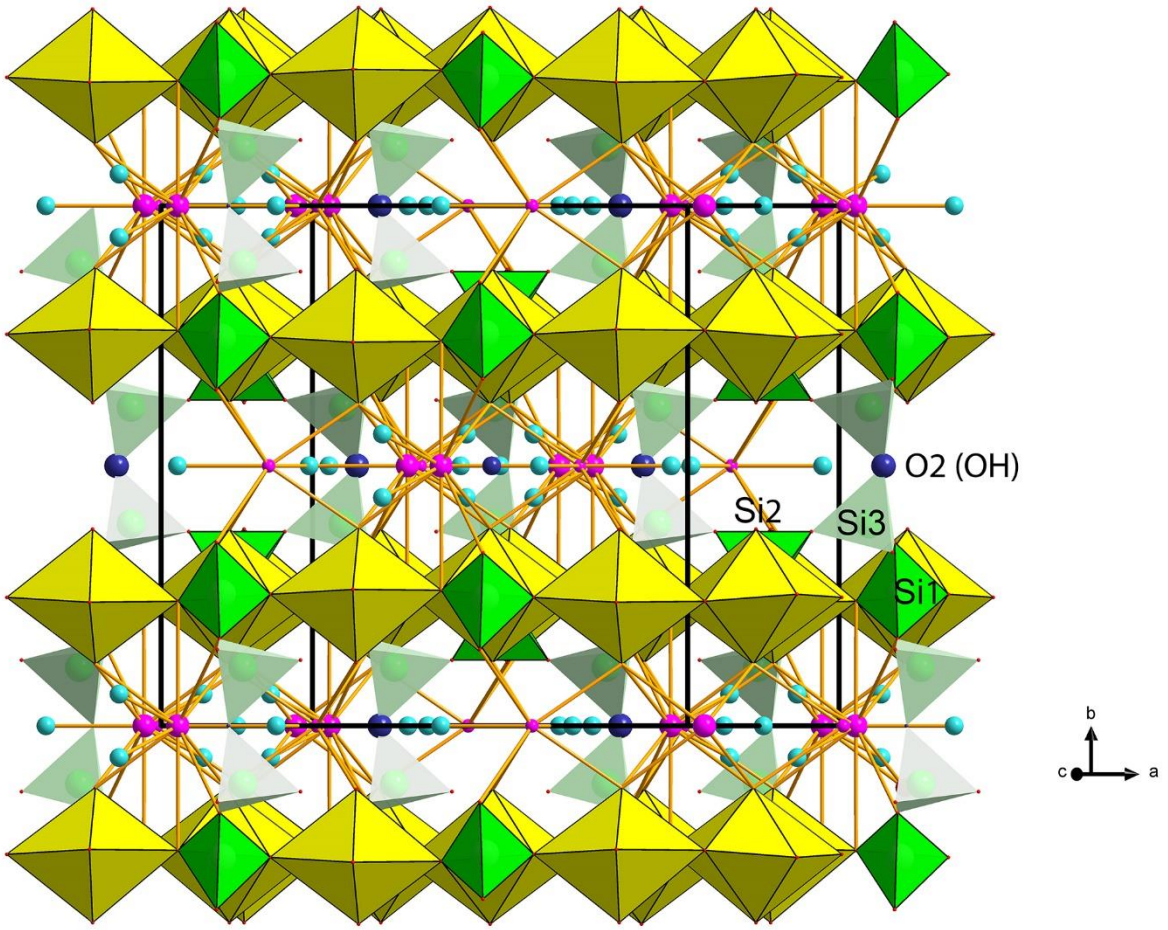

Figure 6. Polyhedral representation of the crystal structure of barronite. The UO_7 bipyramids are in yellow, Si-tetrahedra in green, Ba-sites in purple, H_2O in light blue, O2 atom of the $(OH)^-$ in indigo color. Unit-cell edges are outlined in solid black lines.

https://doi.org/10.1180/mgm.2025.10081 Published online by Cambridge University Press

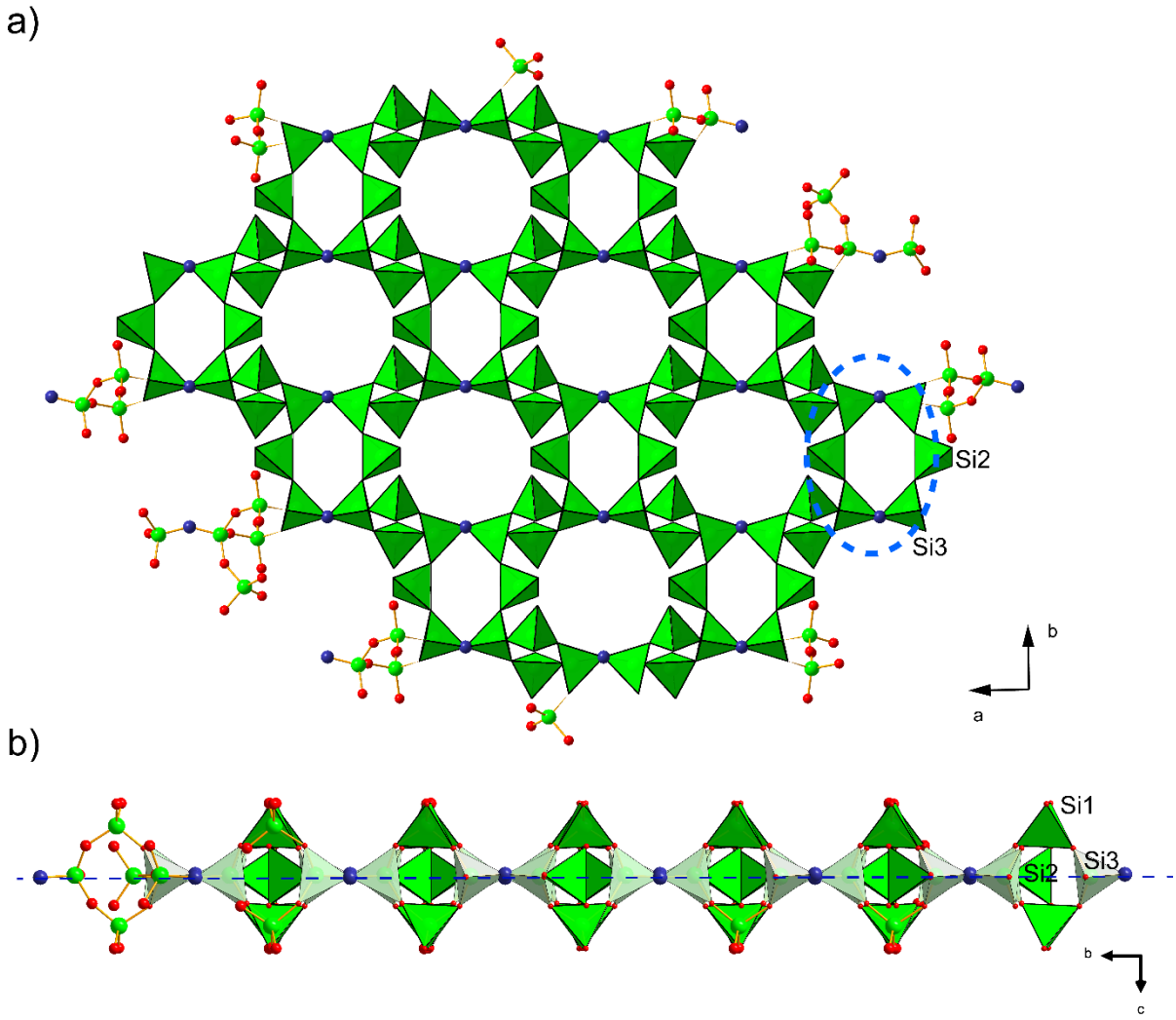

Figure 7. Infinite sheet of Si-tetrahedra (green), composed of six-membered rings (blue dashed line) of vertex-sharing (O2 atom = OH, in indigo color) Si3 and 2×Si2 tetrahedra **(a)**, while Si1 tetrahedra are staggered *"out-of-the plane"* (indicated by long dashed blue line) of those rings **(b)**. The smaller 6-membered rings host only H_2O, while larger rings belong to the cavities with alkaline earth and alkali cations in the weeksite-type structures.

https://doi.org/10.1180/mgm.2025.10081 Published online by Cambridge University Press

TABLE CAPTIONS

Table 1. Chemical composition (wt.%) of barronite.

Constituent	Mean	Range	Stand. Dev.	Reference Material
BaO	5.39	4.96–6.03	0.21	barite
K_2O	0.79	0.33–1.03	0.21	sanidine
PbO	0.55	0.45–0.66	0.06	vanadinite
CaO	0.49	0.34–0.57	0.06	fluorapatite
FeO	0.08	0.04–0.11	0.02	almandine
UO_3	57.97	56.90–59.13	0.57	synthetic UO_2
SiO_2	30.52	30.09–30.93	0.24	sanidine
H_2O*	4.59			
Total	**100.38**			

* calculated by stoichiometry (H = 5 *apfu*).

https://doi.org/10.1180/mgm.2025.10081 Published online by Cambridge University Press

Table 2. X-ray powder diffraction data (*d* in Å) for barronite; the six strongest diffractions are reported in bold.

$I_{obs.}$	$d_{obs.}$	$d_{calc.}$	$*I_{calc.}$	*h*	*k*	*l*	$I_{obs.}$	$d_{obs.}$	$d_{calc.}$	$*I_{calc.}$	*h*	*k*	*l*
63	**8.960**	8.9513	73	0	0	1			1.9018	6	-6	2	4
1	7.696	7.6817	5	-1	1	1	10	1.9015	1.9016	6	6	2	1
100	**7.104**	7.0952	100	0	2	0			1.9013	5	-2	6	3
1	6.600	6.5985	2	-2	0	1			1.9013	5	2	6	2
44	**5.564**	5.5603	29	0	2	1	6	1.8927	1.8927	6	0	4	4
10	4.836	4.8319	3	-2	2	1	4	1.8695	1.8694	4	-6	4	3
		4.8316	8	2	2	0			1.8692	4	6	4	0
20	4.570	4.5680	16	-2	0	2	3	1.8289	1.8291	3	-4	2	5
		4.5673	11	2	0	1			1.8288	3	4	2	3
4	4.477	4.4756	5	0	0	2	5	1.7900	1.7903	5	0	0	5
23	3.842	3.8408	15	-2	2	2	6	1.7743	1.7744	4	-8	0	2
		3.8404	20	2	2	1			1.7738	7	0	8	0
45	**3.550**	3.5489	26	-4	0	1	3	1.7402	1.7400	4	0	8	1
		3.5476	21	0	4	0	4	1.7356	1.7359	4	0	2	5
32	**3.299**	3.2980	34	0	4	1	3	1.7253	1.7250	6	-6	4	4
23	3.197	3.1970	15	-2	0	3			1.7248	6	6	4	1
		3.1966	15	2	0	2	4	1.7219	1.7214	7	-8	2	2
31	3.175	3.1740	43	-4	2	1			1.6871	2	-6	2	5
4	3.124	3.1246	4	-2	4	1	5	1.6864	1.6868	2	6	2	2
12	2.993	2.9916	10	-4	2	2			1.6867	4	-2	6	4
		2.9914	11	4	2	0			1.6866	5	2	6	3
10	2.984	2.9838	5	0	0	3	2	1.6536	1.6535	2	-2	8	2
37	**2.915**	2.9148	23	-2	2	3	4	1.5980	1.5983	2	4	0	4
		2.9145	25	2	2	2			1.5983	2	0	4	5
2	2.803	2.8019	2	-2	4	2	3	1.5869	1.5870	3	-8	4	2
4	2.510	2.5090	7	-4	4	1			1.5867	3	-4	8	1
3	2.4161	2.4159	3	-4	4	2	3	1.5605	1.5600	2	-6	4	5
		2.4158	2	4	4	0			1.5598	2	6	4	2
7	2.4063	2.4062	5	-2	0	4	3	1.5591	1.5594	3	-4	2	6
		2.4060	4	2	0	3			1.5592	3	4	2	4
6	2.3751	2.3749	7	-2	4	3	2	1.5511	1.5511	3	-2	8	3
		2.3748	6	2	4	2			1.5510	2	2	8	2
4	2.3655	2.3651	5	0	6	0	2	1.5154	1.5155	2	-6	6	4
4	2.2864	2.2866	5	0	6	1			1.5154	2	6	6	1
6	2.2784	2.2787	6	-2	2	4			1.4278	3	-2	8	4
		2.2785	7	2	2	3	4	1.4276	1.4277	2	2	8	3
6	2.2377	2.2378	5	0	0	4			1.4274	2	0	6	5
6	2.1996	2.1995	6	-6	0	3	1	1.4193	1.4194	2	-8	6	2
		2.1992	5	6	0	0	3	1.4015	1.3999	2	-6	6	5
5	2.1342	2.1342	5	0	2	4	2	1.3807	1.3807	2	-6	8	3
7	2.1008	2.1009	3	-6	2	3			1.3807	3	6	8	0

https://doi.org/10.1180/mgm.2025.10081 Published online by Cambridge University Press

		2.1007	3	6	2	0			1.3194	3	-6	8	4
		2.1003	5	-2	6	2	3	1.3190	1.3193	3	6	8	1
		2.1002	5	2	6	1	1	1.3170	1.3176	2	-4	10	1
6	1.9915	1.9914	4	-2	4	4			1.2974	2	-10	2	5
		1.9912	3	2	4	3	5	1.2970	1.2973	2	10	2	0
6	1.9738	1.9741	7	-6	0	4			1.2970	2	2	10	2
		1.9738	8	6	0	1	2	1.2605	1.2600	2	0	8	5
2	1.9679	1.9681	8	-4	6	1							
5	1.9224	1.9222	5	-4	6	2							
		1.9221	5	4	6	0							

*$I_{calc.}$ - intensity calculated using the software *PowderCell*2.3 (Kraus and Nolze, 1996) on the basis of the structural model given in Table 4.

https://doi.org/10.1180/mgm.2025.10081 Published online by Cambridge University Press

Table 3. Summary of data collection conditions and refinement parameters for barronite.

Refined structural formula (without hydrogen)	$(\square_{1.286}Ba_{0.409}Ca_{0.084}K_{0.221})_{\sum 2.000}(UO_2)_2Si_5O_{12}(OH)(H_2O)_{1.965}$
Crystal System	Monoclinic
Temperature	94K
a	14.2115(11) Å
b	14.01692(19) Å
c	9.6545(8) Å
β	111.59(6) °
V	1788.2(8) $Å^3$
Z	4
Density [$g \cdot cm^{-3}$] (without H, as refined)	3.6701
Density [$g \cdot cm^{-3}$] (with H)	3.6886
Space group	*C2/m*
F_{000}	459.359
TEM	FEI Tecnai G2 20
Measurement method	Precession assisted 3D ED
Radiation (wavelength)	electrons (0.0251 Å)
Precession angle/tilt step/ total *α*-tilt (°)	1/1/127
Rocking curve width (Å^{-1}), mosaicity (°)(PETS2)	0.0011/0.038
Resolution range (θ)	0.07–1.37
Limiting Laue indices	*h*: –26→26, *k*: 0→22, *l*: 0→18
No. of independent reflections (obs/all) – kinematic	2889/4628
R_{int} (obs/all) – kinematic	0.1362/0.1451
Redundancy	3.433
Coverage for $\sin\theta_{max}/\lambda = 0.8$ $Å^{-1}$	76%
Two-fold axis in direction (104) twinning: *fract1/fract2*	0.7/0.3
Dynamical refinement	
Tot. No. of collected reflections (obs/all)	21022/65039
Reflection selection criteria RSg(max)	0.5
Outliers |Fobs-Fcalc|>10σ(Fobs)	27
No. of reflections (obs/all) (refinement)	6596/15684
R, wR (obs);	0.0791/0.0811
R, wR (all);	0.1380/0.0864
GOF(obs)/GOD(all)	0.0202/0.014
N refined param. all/structural	193/68
Effective thicknesses; variation model	1189(7) Å; wedge
Incoherent mosaicity; simulation steps	0.065; 5
Speed up methods	Bethe potential & scattering cluster approximation

https://doi.org/10.1180/mgm.2025.10081 Published online by Cambridge University Press

Table 4. Atom positions and isotropic displacement parameters (in Å^2) for barronite.

Atom	*Wyck.*	*Occ*	*x*	*y*	*z*	U_{iso}
U1	8j	1	0.40062(7)	0.25443(10)	0.10276(4)	0.00784(9)
Si1	8j	1	0.6864(3)	0.2461(5)	0.24826(17)	0.0062(3)
Si2	4h	1	0.5	0.1987(4)	0.5	0.0077(6)
Si3	8j	1	0.7003(2)	0.1121(3)	0.4974(4)	0.0120(5)
Ba1	4i	$Ba_{0.170(4)}Ca_{0.0348(8)}K_{0.092(2)}$	0.2443(5)	0.5	0.1384(7)	0.0083(16)
Ba2	4i	$Ba_{0.239(5)}Ca_{0.0491(11)}K_{0.129(3)}$	0.4293(4)	0.5	-0.1345(6)	0.0246(19)
O1	8j	1	0.4016(6)	0.3810(8)	0.0920(7)	0.0314(15)
O2	4i	1	0.7306(6)	0	0.5081(14)	0.047(2)
O3	8j	1	0.7470(3)	0.2470(7)	0.1374(5)	0.0100(6)
O4	8j	1	0.7149(6)	0.3331(7)	0.3604(6)	0.0278(12)
O5	8j	1	0.3999(6)	0.1219(7)	0.1034(6)	0.0240(13)
O6	8j	1	0.5711(4)	0.2606(7)	0.1341(5)	0.0104(8)
O7	8j	1	0.7055(4)	0.1468(5)	0.3476(4)	0.0100(6)
O8	8j	1	0.5897(4)	0.1265(5)	0.4944(8)	0.0279(11)
O9	8j	1	0.5349(4)	0.2623(6)	0.6493(3)	0.0151(7)
O10	4i	0.84(4)	0.2322(10)	0.5	-0.1711(15)	0.053(5)
O11	4i	0.45(3)	-0.0603(18)	0.5	-0.101(3)	0.053(5)
O12	2c	0.652(18)	0	0	0.5	0.013(2)
O13	8j	0.174(9)	0.4661(18)	0.561(3)	-0.395(2)	0.013(2)

https://doi.org/10.1180/mgm.2025.10081 Published online by Cambridge University Press

Table 5. Selected interatomic distances (in Å) in barronite.

U1–O1	1.777(11)	Si1–O3	1.602(6)	Si2–O8	1.645(8)
U1–O3	2.492(5)	Si1–O4	1.582(9)	Si2–O8	1.645(8)
U1–O3	2.327(5)	Si1–O6	1.616(5)	Si2–O9	1.610(6)
U1–O5	1.857(9)	Si1–O7	1.655(8)	Si2–O9	1.610(6)
U1–O6	2.330(5)	<Si1–O>	1.614	<Si2–O>	1.627
U1–O6	2.465(5)				
U1–O9	2.229(3)				
<U1–O_{Ur}>	1.817				
<U1–O_{eq}>	2.369				

	Ba1–O1	2.952(12)	Ba2–O1	2.890(11)
	Ba1–O1	2.952(12)	Ba2–O1	2.890(11)
	Ba1–O3	3.462(10)	Ba2–O1	2.828(11)
	Ba1–O3	3.462(10)	Ba2–O1	2.828(11)
	Ba1–O5	3.008(9)	Ba2–O4	3.338(9)
	Ba1–O5	3.008(9)	Ba2–O4	3.338(9)
	Ba1–O7	3.072(8)	Ba2–O6	3.356(10)
	Ba1–O7	3.072(8)	Ba2–O6	3.356(10)
	Ba1–O10	2.929(16)	Ba2–O10	2.691(16)
	Ba1–O11	2.50(3)	Ba2–O12	2.88(3)
			Ba2–O12	2.88(3)
	<Ba1–O>	3.042	<Ba2–O>	3.068

https://doi.org/10.1180/mgm.2025.10081 Published online by Cambridge University Press

Table 6. Bond-valence analysis of the barronite structure (in valence units, *vu*).

	U1	Si1	Si2	Si3	Ba1	Ba2	sum^{-H}	assignment	sum^{+H}	theor[H]	nH$_2$O
O1	1.76				0.17$^{\times 2\downarrow}$	0.19$^{\times 2\downarrow}$, 0.23$^{\times 2\downarrow}$	2.14	O			
O2				1.01		0.04	1.05	OH	1.80		
O3	0.39, 0.55	1.06			0.05$^{\times 2\downarrow}$		2.05	O			
O4		1.12		0.95		0.06$^{\times 2\downarrow}$	2.13	O			
O5	1.86				0.14$^{\times 2\downarrow}$		2.00	O			
O6	0.55, 0.41	1.02				0.06$^{\times 2\downarrow}$	2.04	O			
O7		0.92		1.20	0.12$^{\times 2\downarrow}$		2.25	O			
O8			0.95$^{\times 2\downarrow}$	1.14			2.09	O			
O9	0.68		1.04$^{\times 2\downarrow}$				1.72	O	1.92	1	
O10					0.18	0.32	0.50	H$_2$O	2.10		0.84
O11					0.51		0.51	H$_2$O	2.11		0.45
O12						0.20$^{\times 2\downarrow}$	0.20	H$_2$O	1.80	1	0.33
O13							0.00	H$_2$O	1.60	2	0.35
sum	6.20	4.12	3.97	4.29	1.64	1.84					1.96

* Bond-valence parameters are from Gagné and Hawthorne (2015). sum^{-H} – the sum of the BV without the contribution of the H-bonds; sum^{+H} – the sum of the BV including assumed H-bonds (considering the theoretical H-bond strength of 0.8 *vu* for the *D*–H bond; after Brown, 2002); theor [H] – theoretical number of additional weak H-bonds that the Oatom could accept (considering the theoretical H-bond strength of 0.2 *vu* for the H–*A* bond; after Brown, 2002); *n* H$_2$O–number of H$_2$O molecules/cell, considering site-multiplicities and *Z* = 4. Site occupancies at the Ba1 and Ba2 sites were not taken into consideration.

Table 7. Uranyl silicate minerals and their complexity measures including H atoms.

Mineral	**References**	**Spgr.**	***V* [Å]**	***v***	**I_G [bits/atom]**	**$I_{G,total}$ [bits/unit cell]**	**I_{Chem} [bits/formula]**

https://doi.org/10.1180/mgm.2025.10081 Published online by Cambridge University Press

Soddyite	[1]	*Fddd*	1740	34	2.44	82.97	26.27
Boltwoodite	[2]	$P2_1/m$	321	32	3.75	120.00	27.11
Sklodowskite	[3]	*C*2/*m*	779	37	3.80	140.75	58.22
Cuprosklodowskite	[4]	*P*–1	384	37	4.24	156.75	60.39
Kasolite	[5]	$P2_1/c$	596	48	3.59	172.08	21.37
Oursinite	[6]	*Cmce*	2860	74	3.80	281.50	58.91
Uranophane	[7]	$P2_1$	736	68	5.09	345.95	56.47
Weeksite	[8]	*C*2/*m*	1809	82	4.70	385.32	67.57
Barronite	this paper	*C*2/*m*	1788	88	4.66	410.43	61.64
Parauranophane	[9]	$P2_1/c$	1428	136	5.09	691.90	56.47
Haiweeite	[10]	*Pbcn*	4667	408	5.67	2314.35	77.13
Swamboite-(Nd)*	[11]	$P2_1/n$ – *b* setting	14390	1248	10.29	12836.18	25.39
Lepersonnite-(Gd)#	[12]	*Pmnn*	7563	380	5.896	2240.45	231.88

[1] – Demartin *et al.* (1992), [2] – Burns (1998), [3] – Ryan and Rosenzweig (1977), [4] – Rosenzweig and Ryan (1975), [5] – Fejfarová *et al.* (2013), [6] – Kubatko and Burns (2006), [7] – Ginderow (1988), [8] – Fejfarová *et al.* (2012), [9] – Viswanathan and Harneit (1986), [10] – Plášil *et al.* (2013), [11] – Plášil *et al.* (2018), [12] – Plášil *et al.* (2025).

* – referring to the superstructure (commensurate modulation); the space group transformed into a standard setting *via* matrix (–0.5, 0, –0.5| 0, –1, 0| –0.5, 2, 0.5)

–updated formula of lepersonnite-(Gd), which is carbonate-silicate, is $[Ca_{0.5}Gd_{0.5}(H_2O)_{18}(OH)_{1.5}][Gd(UO_2)_{12}(SiO_3OH)_2(CO_3)_4(OH)_{10}O_2(H_2O)_5]$.

https://doi.org/10.1180/mgm.2025.10081 Published online by Cambridge University Press